www.czasopisma.pan.pl PAN POLSKA AKADEMIA NAUK www.journals.pan.pl

ARCHIVES OF ELECTRICAL ENGINEERING VOL. 64(4), pp. 535-546 (2015)

DOI 10.1515/aee-2015-0039

Electromagnetic launch systems for civil aircraft assisted take-off

LUCA BERTOLA, TOM COX, PATRICK WHEELER, SEAMUS GARVEY, HERVE MORVAN

The University of Nottingham
Institute for Aerospace Technology
Triumph Road, NG7 2TU, Nottingham, United Kingdom
e-mail: luca.bertola@nottingham.ac.uk

(Received: 23.08.2015, revised: 20.09.2015)

Abstract: This paper considers the feasibility of different technologies for an electromagnetic launcher to assist civil aircraft take-off. This method is investigated to reduce the power required from the engines during initial acceleration. Assisted launch has the potential of reducing the required runway length, reducing noise near airports and improving overall aircraft efficiency through reducing engine thrust requirements. The research compares two possible linear motor topologies which may be efficaciously used for this application. The comparison is made on results from both analytical and finite element analysis (FEA).

Key words: civil aircraft launch, electromagnetic launch system, linear induction motor, linear permanent magnet synchronous motor

1. Introduction

The engine size of modern aircraft is principally determined by take-off conditions, since initial acceleration requires maximum engine power. An Electromagnetic Launch (EML) system could provide some or all of the entire energy required at the launch stage so that the engine power requirement and fuel use may be significantly reduced [1]. In the hypothesis of a launch system supplying all the energy required to accelerate the aircraft, all the fuel consumed to take-off can be saved. For instance, considering the data of the CFM56-5B4 engine [2] usually mounted on the Airbus A320-200, the total fuel burnt during take-off can be computed as indicated in Equation (1)

$$\textit{Fuel burnt} = 2\ \textit{engines} \cdot 1.166\ \text{kg/s} \cdot 42\ \text{s} = 97.94\ \text{kg}. \tag{1}$$

Even though the propellant saved in single flight is just a small portion of the total amount of fuel on board the aircraft at the departure, considering an airport like Heathrow with approximately 650 flights per day, about 63.661 kg of fuel can be saved on a daily basis. Considering

the engine emission indices per kilo reported in Table 1, it is possible to estimate the daily exhaust emission reduction. The NOx emission in Table 1 is equivalent to the daily emission of 80,180 diesel cars [3].

Table 1. Exhaust emission reduction

Pollutant	HC	CO	NOx
Emission indices [g/kg] [2]	0.397	0.397	28.7
Daily emission reduction [kg]	6.37	31.83	1827.07

Aircraft engines usually take 4-5 seconds to pass from idle condition to maximum power. Comparing this time with the usual 42 s required by an Airbus A320 to take-off, approximately 88% noise emission reduction at ground level may be expected. This noise emission will occur only near the point of take-off, not along the entire runway length.

The thrust level that can be delivered by an EML system allows for accelerations that cannot be reached by aircraft engines. Consequently, EML systems have the potential of significantly reduce the nominal runway length required by the aircraft to take-off. Expensive airport extensions to face constant air traffic growth could be avoided by allowing large aircraft to operate from short runways at small airports.

So far, EML has been adopted only for military applications to replace steam catapults on the deck of aircraft carriers [4, 5]. This paper will describe the application of EML to propel civil aircraft on the runways of modern airports. The machine topologies mainly considered for EML are Linear Induction Motor (LIM) [6], and Permanent Magnet Linear Synchronous Motor (LPMSM) [7]. The design and the comparison of the two topologies to launch an A320 are presented.

2. Launcher requirements

General Atomics developed an EML system that is able to launch aircraft up to an F-35C in weight [4]. In Table 2 requirements for this machine are compared with those for the launch of an A320. The masses in Table 1 are aircraft Maximum Take-Off Weights (MTOW).

Table 2. List of requirements

Requirements	F-35C [4]	A320 [8]
Aircraft mass	37000 kg	73 500 kg
Take-off speed	78 m/s	70 m/s
Acceleration	3.3 G	0.6 G
Peak Thrust	1.198 MN	0.548 MN
Runway length	94 m	535 m
Launch energy	113 MJ	182 (210) MJ
Take-off time	2.4 s	12 s

FAR and JAR international regulations consider as take-off speed V_2, the minimum calibrated air speed at 35 ft above the runway, while the speeds in Table 2 are the rotation speeds V_R, i.e. the minimum calibrated air speed at which aircraft nose can be rotated [9]. The rotation speed V_R is approximately 95% of the take-off speed V_2 according to Equation (2).

$$V_R = \frac{1.05\,V_2}{1}. \tag{2}$$

The runway lengths in Table 2 were simply computed assuming a uniformly accelerated motion to the rotation speed and a safety distance as specified in [10].

Most of civil aircraft accelerate at 0.3 G since the maximum engines thrust is about 30-35% the MTOW [8]. In order to shorten the runway length, an acceleration of 0.6 G was chosen, as this will give an increased acceleration without being uncomfortable to the passenger over 12 s, i.e. the take-off time assuming an acceleration of 0.6 G as reported in Table 2.

There are no regulations in aviation which limit the maximum axial take-off acceleration for passengers, but appropriate levels must be chosen that are both safe and comfortable. This work has taken acceleration standards from the American Society for Testing and Materials, which developed standards for allowable acceleration in amusement rides [11]. According to Fig. 1 the maximum axial acceleration that can be withstood for 12 s is 2.5 G, significantly more than the 0.6 G chosen.

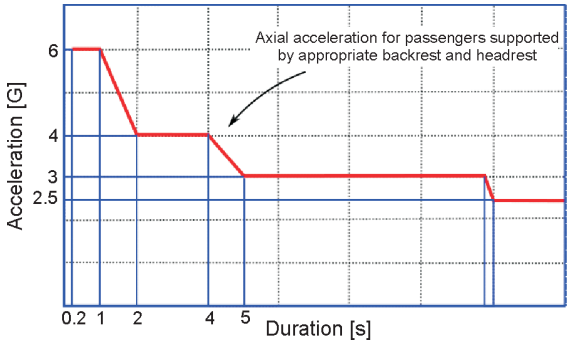

Fig. 1. Acceleration limits for aircraft passengers [11]

Since the dimensions of aircraft carriers are established, the acceleration for the F35-C is a function of the runway length and of the take-off speed. On the contrary, the acceleration of the civil aircraft is given and the runway is subsequently computed. Therefore, even though the aircraft mass is lower, the thrust the catapult has to deliver to accelerate the military jet is more the two times greater than that needed for the civil aircraft.

The F-35C launch energy in Table 2 [1] was computed considering the thrust to accelerate the aircraft mass only. The same was done for the A320, but the energy contributions of aerodynamic drag and ground friction were considered as well and reported in Table 1 within brackets.

The A320 peak thrust occurs at the end of the acceleration path considering the aerodynamic drag and the ground friction. The force requirement for the A320 launcher can be seen in Fig. 2, along with its constituent parts.

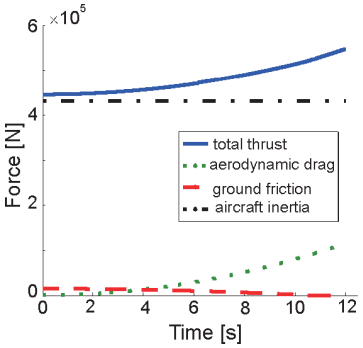

Fig. 2. Forces acting on A320 during take-off at 0.6 G constant acceleration

3. Electromagnetic catapult

The sizing procedure of both LIM and LPMSM has been developed highlighting the key aspects. The main results are then reported for both the electric motors.

3.1. Linear induction motor

A multistage design procedure was adopted for a double-sided long primary LIM (active guideway). This topology was chosen to avoid full power transfer on board and to have little to no normal force between stators and rotor. In each stage the distributed windings are fed with increasing frequency while the reaction plate is moving, in order to maintain an optimal thrust and minimal slip level. The reaction plate is made out of aluminum for its low density, high strength (vs copper) and high electrical conductivity.

The starting point of the EML design is the thrust requirement for the launch of an A320 in Table 2. The pole pitch τ, the stack width w, the airgap length g, the aluminum thickness d_{Al} and the number of active pole pairs p were selected through a graphic optimization procedure to maximize the power factor $cos\varphi$ and the efficiency η of the machine.

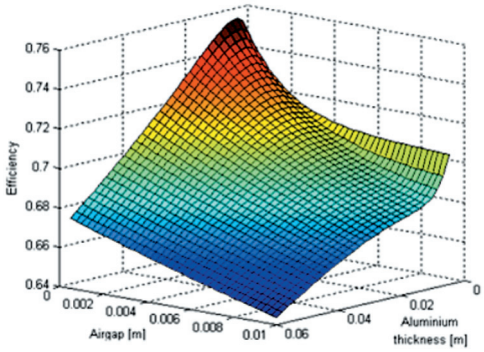

Fig. 3. Airgap and aluminum thickness effect on the efficiency

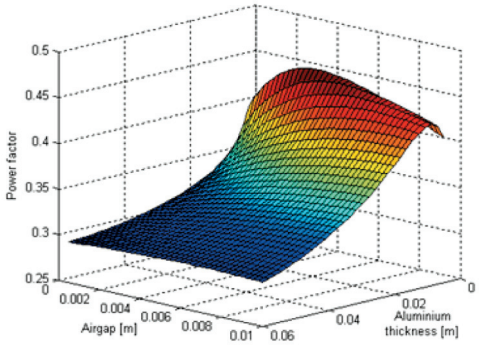

Fig. 4. Airgap and aluminum effect on power factor

The adopted optimization procedure consists in graphic visualization of the effects of the variation of two parameters, while all the others are kept constant as can be seen in Fig. 3 and Fig. 4. Even though it is not the most precise optimization method, it was ideal for the preliminary design since it is intuitive, easy to implement and it rapidly leads to a feasible solution. Once the arrays of values of two parameters are given the machine performance is computed with the following algorithm.

1. Calculation of the goodness factor [12]

$$Gf = \frac{\mu_0 \cdot \tau^2 \cdot \omega_1 \cdot \sigma_{A1} \cdot d_{A1}}{\pi^2 \cdot g_e \cdot k_{skin} \cdot k_{tr} \cdot (1 + k_{sat})}, \tag{3}$$

where: μ_0 – void magnetic permeability; ω_1 – primary frequency; σ_{A1} – aluminum electrical conductivity; $g_e = (2g + d_{A1}) \cdot k_c \cdot k_{fg}$ – equivalent airgap length, where k_c is the Carter coefficient and k_{fg} is the fringing factor; k_{skin} – skin effect coefficient; k_{tr} – transverse end effect coefficient; k_{sat} – saturation coefficient.

2. Calculation of the magnetization inductance

$$Lm = \frac{6 \cdot \mu_0 \cdot \tau \cdot (kw_1 \cdot n_1)^2 \cdot w_e}{\pi^2 \cdot p \cdot g_e \cdot (1 + k_{sat})} = k_{Lm} \cdot n_1^2, \tag{4}$$

where: kw_1 – winding factor; n_1 – number of turns per phase; $w_e = w + g_e$ equivalent stack width.

3. Calculation of rated magnetomotive force

$$n_1 I_1 = \sqrt{\frac{F \cdot \tau \cdot (1 + (s \cdot Gf)^2)}{3 \cdot \pi \cdot k_{Lm} \cdot s \cdot Gf}}, \tag{5}$$

where: F – thrust in Table 2; s – slip frequency.

4. Calculation of the average magnetic field density in the airgap

$$B_g = \frac{3\sqrt{2} \cdot \mu_0 \cdot kw_1 \cdot w_1 I_1}{g_e \cdot p \cdot \pi \cdot \sqrt{(1 + (s \cdot Gf)^2)}}, \tag{6}$$

5. Calculation of the efficiency and power factor including end effects

$$\eta = \frac{[F_{Mag} \cdot (1 - k_{ef}) - F_a] \cdot (1 - s) v_s}{F \cdot v_s + 3 \cdot R_1 \cdot I_1^2 + P_{core} + P_{ef}} = \frac{\eta_{num}}{\eta_{den}}, \tag{7}$$

$$\cos\varphi = \frac{\eta_{den}}{\sqrt{\eta_{den}^2 + (3 \cdot \omega_1 \cdot L_1 \cdot I_1^2 + Q_{ef})^2}}, \tag{8}$$

where: F_{Mag} – total thrust produced by the machine; F_a – thrust to accelerate the armature mass; V_s – synchronous speed; R_1, $L_1 = L_m + L_{1L}$ – primary resistance and inductance respectively; P_{core} – power wasted in the core; k_{ef}, P_{ef}, Q_{ef} – thrust reduction, additional secondary losses and additional absorbed reactive power due to dynamic end-effect respectively [13].

To model the dynamic behavior of the machine, the LIM equivalent circuit with an additional resistance Re in parallel and a modified magnetization inductance was used as shown in Fig. 5 [14]. The classic equivalent circuit for rotary induction machine was modified in this way to take into account specific LIM phenomena like end-effect and edge effects.

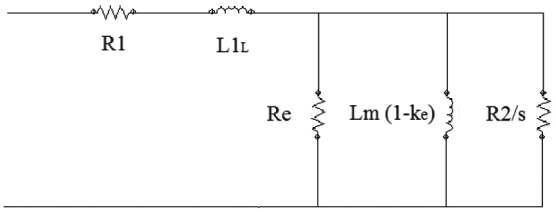

Fig. 5. LIM equivalent circuit

The dynamic behavior of the machine has been modelled using the system of Equations (9)-(15) and the solution has been compared with FEA (Fig. 6), showing a good agreement even with varying frequency. Further details of the design are shown in Section 4.

$$V_1 = R_1 \cdot I_1 + \frac{\partial \Psi_1}{\partial t} + j \cdot \omega_1 \cdot \Psi_1, \tag{9}$$

$$0 = R_2 \cdot I_2 + \frac{\partial \Psi_2}{\partial t} + j \cdot (\omega_1 \cdot \omega_r) \cdot \Psi_1, \tag{10}$$

$$0 = R_e \cdot I_e - \frac{\partial \Psi_m}{\partial t}, \tag{11}$$

$$\Psi_1 = L_1 \cdot I_1 + \Psi_m, \tag{12}$$

$$\Psi_2 = \Psi_m, \tag{13}$$

$$\Psi_m = L_m \cdot (1 - k_e) \cdot I_m, \tag{14}$$

$$\omega_r = \frac{\pi}{\tau} \cdot v_s \cdot (1 - s). \tag{15}$$

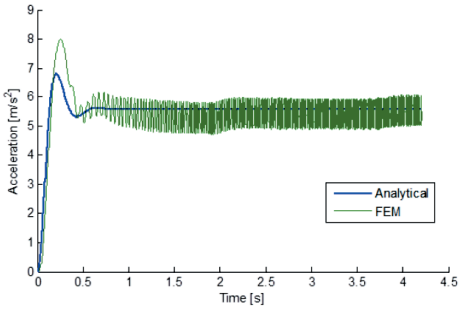

Fig. 6. Circuit model and FEA results comparison

3.2. Linear permanent magnet synchronous motor

The machine is a double-sided long stator LPMSM with fractional tooth windings fed with a common increasing frequency. The armature was designed accounting for minimum use of permanent magnet materials to give a cost effective solution for a large number of launches.

The concentrated winding configuration can be more efficient for a segmented stator since transition effects between segments can be neglected. One of the main advantages of this winding configuration is that a correct design leads to a drastic reduction of the cogging force. Moreover, such winding layout is easier to manufacture than a distributed one and has shorter end-windings with consequent reduced Joule losses. Double-layer windings were also considered since they generally produce a more sinusoidal back-emf waveform than single-layer windings. In order to get a tooth winding machine with the highest performance for a given number of slots and poles, a distribution algorithm to select the winding sequence was employed. It is similar to the method proposed in [15] for rotary machines, but with some modifications to adapt it to linear motion and some steps added to allow for software implementation.

1. Selection of the number of poles and slots to get a high winding factor and a low cogging force. The bigger the least common multiple (LCM) of number of poles and number of slots the lower will be the cogging force. The steps will be furter clarified using the data reported in Table 3.

Table 3. Example of number of slots and poles

Slots N_s	Poles $2p$	Phases ph	Winding factor kw	LCM
36	28	3	0.902	252

2. The number of slots per pole per phase q is written as a fraction reduced to the lowest terms: $q = n/d$ where n and d are integers (see Eq. (16)).

$$q = \frac{N_s}{2p \cdot ph} = \frac{36}{28 \cdot 3} = \frac{3}{7} = \frac{n}{d'} \qquad z = d - n = 4, \tag{16}$$

3. The optimal sequence of n "1" and $z = n - d$ "0" has to be found.The minimum number of zeros after each ones is the quotient $mz = z/n$ where mz is an integer number.
4. The number of zeros to redistribute r is the remainder of the ratio z/n.
5. The optimal sequence is initialized as a vector of d zeros while position indexes of the "1" are computed according to (17)

$$\begin{cases} i + (mz+1)\cdot(i-1) & for \quad i = 1, 2, \ldots r \\ i + mz \cdot (i-1) + r & for \quad i = r+1, r+2, \ldots n \\ i + mz \cdot (i-1) & if \quad r = 1, \ and \ \ d \neq 5. \end{cases} \tag{17}$$

In case only one zero has to be redistributed ($r = 1$), it is put at the end of the sequence except when d is equal to 5 (third equation). This is done to group the first phase at the beginning of the sequence (in a rotary machine nothing changes since the edges of the sequence coincide).

When zeros are more than one, they are redistributed starting from the beginning of the sequence. Steps 3 to 5 for the example proposed in Table 3 are reported in Table 4.

Table 4. Optimal binary sequence

Minimum number of 0 after each 1	$mz = z/n = 4/3 = 1$
Number of 0 to b redistributed	Reminder of z/n, $r = 1$
Sequence initialization with d zeros	0 0 0 0 0 0 0
Indexes of the 1 in the sequence. See Eq. (17)	$\text{index}_{i=1\div n} = i + m_z \cdot (i-1) \rightarrow$ index = 1, 3, 5
Optimal sequence of 1 and 0	1 0 1 0 1 0 0

6. The obtained optimal sequence is subsequently repeated three times and compared with classic sequence AC'BA'CB' of distributed windings. The phases associated with a "1" are than selected to form the optimal repeatable winding sequence as shown in Table 5.

Table 5. Optimal repeatable winding sequence

1	0	1	0	1	0	0	1	0	1	0	1	0	0	1	0	1	0	1	0	0
A	C'	B	A'	C	B'	A	C'	B	A'	C	B'	A	C'	B	A'	C	B'	A	C'	B
Optimal repeatable winding sequence										A B C C' A' B' B C A										

7. In case d is odd the sequence is antiperiodic and the transposed sequence of phases must be added as shown in Table 6.
8. The winding sequence has to be repeated to cover all the active slots. The number of repetitions is equal to the great common divisor between the slot number Ns and the number of pole pairs as shown in Table 6.

Table 6. Antiperiodic sequence and number of repetitions

Antiperiodic sequence since d is odd	A B C C′ A′ B′ B C A A′ B′ C′ C A B B′ C′ A′
Number of series repetitions	Rep = $GCD(N_s, p) = 2$

9. The second layer is obtained by closing each phase and shifting it of one slot. The final winding sequence is shown in Table 7.

Table 7. Optimized double layer tooth winding sequence 36 slots 28 poles

A	B	C	C′	A′	B′	B	C	A	A′	B′	C′	C	A	B	B′	C′	A′	A	B	C	C′	A′	B′	B	C	A	A′	B′	C′	C	A	B	B′	C′	A′
	A′	B′	C′	C	A	B	B′	C′	A′	A	B	C	C′	A′	B′	B	C	A	A′	B′	C′	C	A	B	B′	C′	A′	A	B	C	C′	A′	B′	B	C	A

Once the number of poles and slots are selected and the winding sequence determined, multi-layer theory (MLT) is applied to model the machine [16, 17]. MLT allows for the computation of magnetizing inductance and of the overall PM magnetic flux. Fig. 7 shows the magnetic field density distribution along the machine thickness under a pole pair reconstructed by MLT accounting for slotting effect through conformal mapping functions.

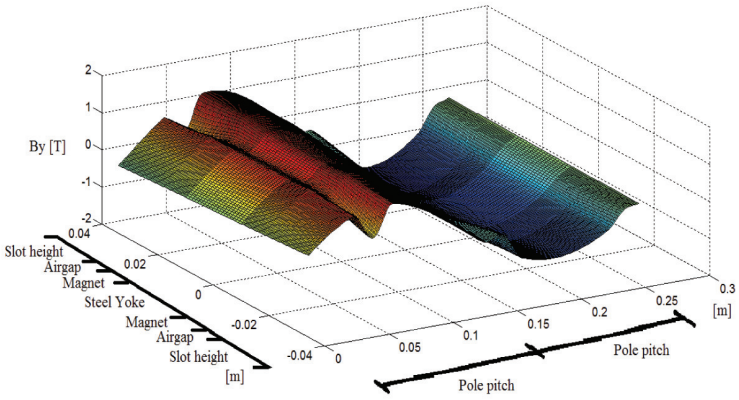

Fig. 7. Field density generated by a pole pair with slotting effect

A proper design leads to a reasonably sinusoidal electromotive force. If cogging forces are treated as disturbances the *dq*-model can be safely applied. The phasor diagram has been used to represent the dynamic behavior of the machine under operative conditions. In the case of tooth winding the model reflects the action of the fundamental electromotive force, while other space harmonics are not considered. Despite the approximation the model provides a good estimation of steady-state and dynamic performance as shown in Fig. 8.

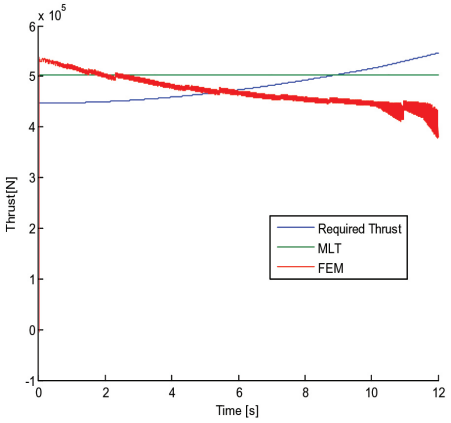

Fig. 8. MLT and FEA results comparison

The machine has been designed considering the thrust required at the end of acceleration (Fig. 8, blue line). From Fig. 8 it can be observed that the MLT result slightly underestimates the permanent magnet flux and therefore it computes a lower thrust than the one required at the end of the track. In any case the take-off speed is reached because the average thrusts are similar. The FEA model predicts the thrust reasonably well, but the output thrust gradually decreases due to the effects of non-linear iron. The thrust predicted by MLT is constant because it assumes linear behavior of the stator material.

4. Results and comparison

The key results from the analytical design are efficiency, power factor and mover mass, the mean values of which are reported in Table 8. High values of efficiency and power factor entail acceptable requirements for power conditioning and energy storage systems. The mass of the plate has to be low to transfer the major quantity of kinetic energy to the aircraft. Table 8 presents other design parameters of both the induction and synchronous machines.

Table 8: Comparison between LIM and LPMSM designs

	LIM	LPMSM
Efficiency	0.853	0.930
Power Factor	0.672	0.893
Armature mass [kg]	308	2662
Pole pitch [m]	0.22	0.1286
Stack width [m]	1.48	1.55
Airgap length [mm]	7	7
Aluminum thickness [mm]	20	–
Magnet thickness [mm]	–	16.2
Magnet length [cm]	–	11.6
Plate width [m]	1.62	–
Slot pitch [cm]	7.33	10
Slot width [cm]	3.7	4.0
Slot height [cm]	2.2	3.3
Poles pair	8	14
Slot per pole per phase	1	3/7
Goodness factor	33.1	–
Average slip frequency	0.13	–
Current density [A/mm^2]	30	10
Thrust density [Pa]	120 000	80 000
Leakage inductance [mH]	3.2	4.2
Magn. inductance [mH]	11.7	2.4
Stator resistance [mΩ]	225	93.2

5. LIM structural instability analysis

The impact of the high LIM thrust density on the aluminum plate has been studied through static and modal structural analysis. The main concern with heavily loaded slender structural components like the LIM armature is buckling instability. The buckling analysis returns the

load factor which is the ratio between the buckling load and the operational load (18). It may be interpreted as the distance between the actual load condition and the instability load.

$$f_b = \frac{\text{Load}_{\text{buckling}}}{F}. \tag{18}$$

The analysis has been carried out with fixed constraints on the plate top edge where the aircraft is connected. Structural performances can be improved adding a guide for the bottom edge which constrains the transversal displacement. The results are reported in Table 9, while plate buckling exaggerated deformation is shown in Fig. 9.

Table 9. Structural analysis results

Parameters	Top edge constrained	Both edges constrained
Max displacement [mm]	0.397	0.397
Max stress [MPa]	30	30
Load factor	5.18	14.67

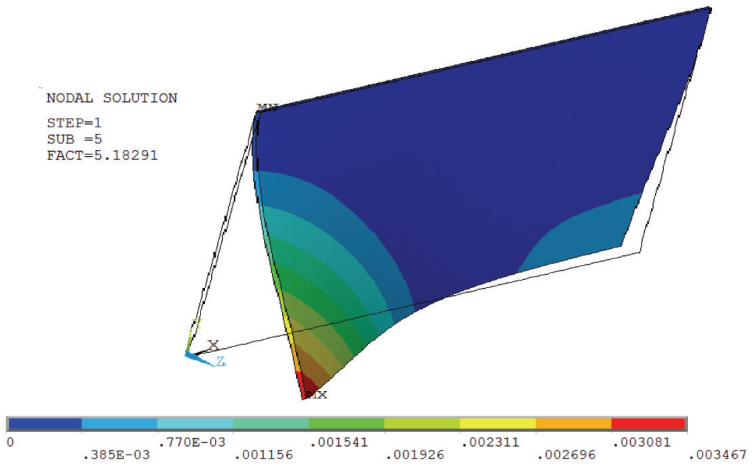

Fig. 9. Exaggerated plate deformation under buckling load

7. Conclusions

Electromagnetic launch for an A320 or similar sized civil aircraft has been proved feasible in terms of actual technology readiness. LIMs present a lower power factor and efficiency than LPMSMs, but they have a lighter mover and lower electric frequency (longer pole pitch).

The thermal behavior of the machines under rated current density needs to be further investigated. However coils are fed for a very short time so strong temperature rises are not expected. In the induction machine, the increment of temperature inside the aluminum plate has been computed balancing the energy loss in the secondary, the heat dissipated by convection and

energy absorbed by the plate itself. A rise in temperature of only 24K per launch was calculated. Nevertheless the losses in plate are not uniform and to compute the exact temperature variation the transversal distribution of current density in the plate needs to be determined.

Even though the launchers presented in this paper are for a class of MTOW only, further studies are ongoing to design induction and synchronous launchers for heavier aircraft like the A380. The gain in terms of runway length reduction is noticeable (Table 2), considering that actual take off distances for A320 and A380 are 2590 m and 2970 m respectively (ISA +20ºC and MTOW). The benefit of the reduction of fuel consumption during take-off is accentuated by the potential decrement of the main engine thrust requirement which could lead to smaller engines with lower specific fuel consumption. The main drawback of the electromagnetic catapult is that it needs to be installed on a large number of airports to take advantage of its benefits.

Acknowledgements

The research leading to these results has received funding from the People Programme (Marie Curie Actions) of the European Union's Seventh Framework Programme (FP7/2007-2013) under REA grant agreement no 608322.

References

[1] Bertola L., Cox T., Wheeler P. et al., *Civil Application of Electromagnetic Aircraft Launch System.* Presented at the LDIA, Aachen (2015).
[2] E.A.S.A. (EASA), *ICAO, Engine Exhaust Emissions Databank, CFM56 -5B4*. (2015).
[3] E.P.A. EPA, *Average Annual Emissions and Fuel Consumption for Gasoline-Fueled Passenger Cars and Light Trucks*. (2008).
[4] Lentijo K., Bellamy G., Watson J., Flint K., *Launch and Recovery using the EMKIT System*. Amercian Society of Naval Engineer (2010).
[5] Atomics G., *EMALS*. Available: http://www.ga.com/emals, October (2014).
[6] Bellamy G., Lewis E., *The Development of Advanced Linear Induction Motor Systems*. presented at the Power Electronics Machines and Drives, Edinburgh (2004).
[7] Patterson D., Monti A., et al., *Design and Simulation of a Permanent-Magnet Electromagnetic Aircraft Launcher.* IEEE Transaction on Industry Applications 41: 566-575, March/April (2005).
[8] Airbus. *Aircraft Characteristics*. Available: http://www.airbus.com/support/ maintenance-engine ering/technical-data/aircraft-characteristics/, October (2014).
[9] *Joint Aviation Requirements, JAR-25 Large Aeroplanes* 25.107 (1989).
[10] *Joint Aviation Requirements, JAR-25 Large Aeroplanes* 25.113 (1989).
[11] ASTM, *Standard Practice for Design of Amusement Rides and Devices.* F2291-13 (2014).
[12] Laithwaite E.R., *Induction machines for special purposes.* Littlehampton Book Services Ltd (1966).
[13] Boldea I., *Linear Electric Machines, Drives, and MAGLEVs Handbook.* CRC Press, Taylor & Francis Group (2013).
[14] Wang K., Shi L., Li Y., *Direct Thrust Control of Linear Induction Motor Considering End Effects*. presented at the LDIA (2007).
[15] Cros J., Viarouge P., *Synthesis of High Performance PM Motors with Concentrated Windings*. IEEE Transaction on Energy Conversion 17: 248-253 (2002).
[16] Deng Z., Boldea I., Nasar S.A., *Fields in Permanent Magnet Linear Synchronous Machines*. IEEE Transaction on Magnetics 2: 107-112 (1986).
[17] Deng I.B.Z., Nasar S.A., *Forces and Parameters of Permanent Magnet Linear Synchronous Machines.* IEEE Transaction on Magnetics 1: 305-309 (1987).